Title
Predominance of ECH wave contribution to diffuse aurora in Earth's outer magnetosphere

Journal
Journal of Geophysical Research Space Physics, 120(1)

ISSN
2169-9380

Authors
Zhang, Xiao-Jia
Angelopoulos, Vassilis
Ni, Binbin
et al.

Publication Date
2015

DOI
10.1002/2014ja020455

Peer reviewed

AGU PUBLICATIONS

JGR

Journal of Geophysical Research: Space Physics

RESEARCH ARTICLE
10.1002/2014JA020455

Key Points:
- The role of ECH waves in driving diffuse aurora is quantified globally
- ECH waves are the dominant driver of diffuse aurora in the outer magnetosphere
- Relative contribution of high-latitude precipitation decreases in active times

Correspondence to:
X.-J. Zhang,
xjzhang@ucla.edu

Citation:
Zhang, X.-J., V. Angelopoulos, B. Ni, and R. M. Thorne (2015), Predominance of ECH wave contribution to diffuse aurora in Earth's outer magnetosphere, *J. Geophys. Res. Space Physics*, *120*, 295–309, doi:10.1002/2014JA020455.

Received 31 JUL 2014
Accepted 17 DEC 2014
Accepted article online 19 DEC 2014
Published online 20 JAN 2015

Predominance of ECH wave contribution to diffuse aurora in Earth's outer magnetosphere

Xiao-Jia Zhang[1,2], Vassilis Angelopoulos[1], Binbin Ni[3], and Richard M. Thorne[2]

[1]Department of Earth, Planetary, and Space Sciences and Institute of Geophysics and Space Physics, University of California, Los Angeles, California, USA, [2]Department of Atmospheric and Oceanic Sciences, University of California, Los Angeles, California, USA, [3]Department of Space Physics, School of Electronic Information, Wuhan University, Wuhan, Hubei, China

Abstract Due to its importance for global energy dissipation in the ionosphere, the diffuse aurora has been intensively studied in the past 40 years. Its origin (precipitation of 0.5–10 keV electrons from the plasma sheet without potential acceleration) has been generally attributed to whistler-mode chorus wave scattering in the inner magnetosphere ($R < \sim 8\ R_E$), while the scattering mechanism beyond that distance remains unresolved. By modeling the quasi-linear diffusion of electrons with realistic parameters for the magnetic field, loss cone size, and wave intensity (obtained from Time History of Events and Macroscale Interactions during Substorms (THEMIS) observations as a function of magnetospheric location), we estimate the loss cone filling ratio and electron cyclotron harmonic (ECH) wave-induced electron precipitation systematically throughout the entire data set, from 6 R_E out to 31 R_E (the THEMIS apogee). By comparing the wave-induced precipitation directly with the equatorially mapped energy flux distribution of the diffuse aurora from ionospheric observations (OVATION Prime model) at low altitudes, we quantify the contribution of auroral energy flux precipitated due to ECH wave scattering. Although the wave amplitudes decrease, as expected, with distance from the Earth, due to the smaller loss cone size and stretched magnetic field topology, ECH waves are still capable of causing sufficient scattering of plasma sheet electrons to account for the observed diffuse auroral dissipation. Our results demonstrate that ECH waves are the dominant driver of the diffuse aurora in the outer magnetosphere, beyond ~8 R_E.

1. Introduction

The diffuse aurora is a belt of weak emissions extending around the entire auroral oval, which supplies the dominant particle energy input into the ionosphere [*Hardy et al*., 1985; *Newell et al*., 2009]. Although both ions and electrons contribute to it, electron precipitation dominates both the number and energy flux of the diffuse auroral precipitation [*Hardy et al*., 1985, 1989; *Newell et al*., 2009]. The diffuse electron precipitation (referred to as "diffuse aurora" hereafter in this study) extends over a latitude range of 5° to 10° within the auroral oval and maps along the magnetic field lines from the outer radiation belts ($L \sim 4$) to the entire central plasma sheet [*Meredith et al*., 2009]. Diffuse aurora exists during various geomagnetic conditions (denoted by *Kp* and *Dst* indices), but it intensifies during active times [*Petrinec et al*., 1999]. As shown in a recent statistical study [*Newell et al*., 2009, 2010], even during low solar wind driving conditions diffuse auroral precipitation is still intense at higher latitudes (66°–72°), which maps to beyond 8 R_E in the magnetosphere.

The source population for the diffuse aurora is hundreds of eV to ~10 keV plasma sheet electrons scattered into the loss cone through resonant wave-particle interactions [*Fontaine and Blanc*, 1983]. Both electrostatic electron cyclotron harmonic (ECH) waves and whistler-mode chorus waves resonate with electrons in this energy range [*Anderson and Maeda*, 1977] and thus have been considered as mechanisms for plasma sheet electron precipitations. However, the relative importance of these two wave modes in driving the diffuse aurora has remained controversial for over 40 years [e.g., *Kennel et al*., 1970; *Lyons*, 1974; *Belmont et al*., 1983; *Roeder and Koons*, 1989; *Horne and Thorne*, 2000; *Meredith et al*., 2000; *Horne et al*., 2003; *Meredith et al*., 2009; *Thorne et al*., 2010; *Ni et al*., 2011a, 2011b, 2012a; *Kurita et al*., 2014].

Recent studies, combining CRRES observations of ECH and chorus wave distributions and theoretical modeling [*Thorne et al*., 2010; *Ni et al*., 2011b, 2011c; *Tao et al*., 2011] have shown that whistler-mode chorus is the dominant driver of the diffuse aurora on the nightside in the inner magnetosphere ($L < \sim 8$), because only chorus can explain the observed pancake electron distribution after electrons at smaller pitch angles have

been scattered into the loss cone. The mechanism of the diffuse auroral precipitation at higher L shells, however, remains unclear. A recent survey of chorus waves using Time History of Events and Macroscale Interactions during Substorms (THEMIS) observations [*Li et al*., 2009] has demonstrated that the occurrence rate of moderately intense chorus emissions ($\geq$10 pT) drops significantly beyond ~8 R_E. Moreover, average wave amplitudes are below a few pT throughout the night-to-dawn sector (beyond ~8 R_E), i.e., insufficient to cause efficient diffuse aurora at this location. On the other hand, moderately strong ECH emissions (~0.1–1.0 mV/m) have been reported to extend up to ~12 R_E [*Roeder and Koons*, 1989; *Ni et al*., 2011c], and may thus drive electron precipitations in these high L shells (8–12). These results reopen the potential importance of ECH waves at high L shells. *Ni et al*. [2012a] evaluated the precipitation flux due to ECH waves in a detailed case study at $L = 11.5$, showing that the resultant auroral brightness agrees with auroral observations at the magnetic foot point. Therefore, ECH emissions may be the potential driver of diffuse aurora beyond ~8 R_E. By modeling the interaction of ECH waves with plasma sheet electrons, *Zhang et al*. [2013] suggested that these waves may still exist beyond ~12 R_E, although their amplitudes are possibly below detection levels. Wave contribution to scattering would still remain significant due to the smallness of the loss cone size at those large distances.

The impact of ECH waves on the plasma sheet electron dynamics and the diffuse auroral precipitation has not been investigated systematically and globally, however. This requires quantification of quasi-linear bounce-averaged scattering rates and loss timescales of electrons based on a realistic magnetic field topology, wave characteristics, and simultaneous electron distributions. The extensive THEMIS wave and particle databases allow us to develop an improved global model of ECH waves, loss cone size, and the accompanying electron distributions. By modeling the electron diffusion due to interactions with ECH waves, we can estimate the loss cone filling ratio of the local electron distribution and the resultant precipitating energy flux at different regions of the magnetosphere. The contribution of ECH waves to the diffuse auroral precipitation can then be directly investigated by comparing to the overall diffuse auroral precipitation in each location.

For the purposes of this study, we define the "inner magnetosphere" as the region with equatorial crossings <8 R_E and "outer" as that beyond 8 R_E.

We present specifics of our modeling of diffuse auroral precipitation from the ionosphere in section 2 and the methodology to model ECH wave scattering of plasma sheet electrons in section 3. Comparisons of wave-induced precipitating energy flux estimates with diffuse auroral precipitations are shown in section 4. We summarize and discuss our findings in section 5.

2. Modeling Diffuse Auroral Precipitation

We examine the global pattern of diffuse auroral precipitation in the ionosphere using the OVATION Prime model [*Newell et al*., 2009, 2010]. The model is based on 22 years (1984–2005) of energetic particle measurements from the Defense Meteorological Satellite Program (DMSP) from which an empirical relationship between the solar wind conditions and the location and intensity from different types of aurora was developed. Using this model, *Newell et al*. [2009, 2010] have shown that the pattern of diffuse auroral precipitation varies with solar wind driving conditions and that the hemispheric power (globally integrated total particle energy deposition) undergoes small seasonal variations.

As inferred by integration of the energy flux distributions in Figure 1, the hemispheric power of diffuse aurora increases from 5.5 GW to 15.5 GW from low to high solar wind driving conditions. The definition of low and high solar wind driving conditions is the same as used by *Newell et al*. [2009, 2010]. In that figure, we map the diffuse auroral precipitation to the magnetic equator, using both T89 ($Kp = 2$ for low solar wind driving; $Kp = 3$ for high solar wind driving) and T96 (solar wind dynamic pressure $P_{dyn} = 1.6$ nPa; $Dst = -2$ nT; $B_y = 0.5$ nT; $B_z = -1.0$ nT for low solar wind driving; $P_{dyn} = 3.2$ nPa; $Dst = -25$ nT; $B_y = 0.5$ nT; $B_z = -1.0$ nT for high solar wind driving) magnetic field models [*Tsyganenko*, 1989; *Tsyganenko*, 1995, 1996]. For consistency, we use the lower (upper) quartile of P_{dyn} and Dst (OMNI data) from 1988 to 1998 (the same interval with what was used by *Newell et al*. [2009, 2010]) for low (high) solar wind driving conditions. Note that the winter-to-summer ratio of diffuse auroral energy fluxes is close to 1.0; it can be at most ~1.3, during high solar wind driving conditions [*Newell et al*., 2010], so we use the energy flux precipitation during local summer conditions to represent the global pattern of diffuse aurora in these plots.

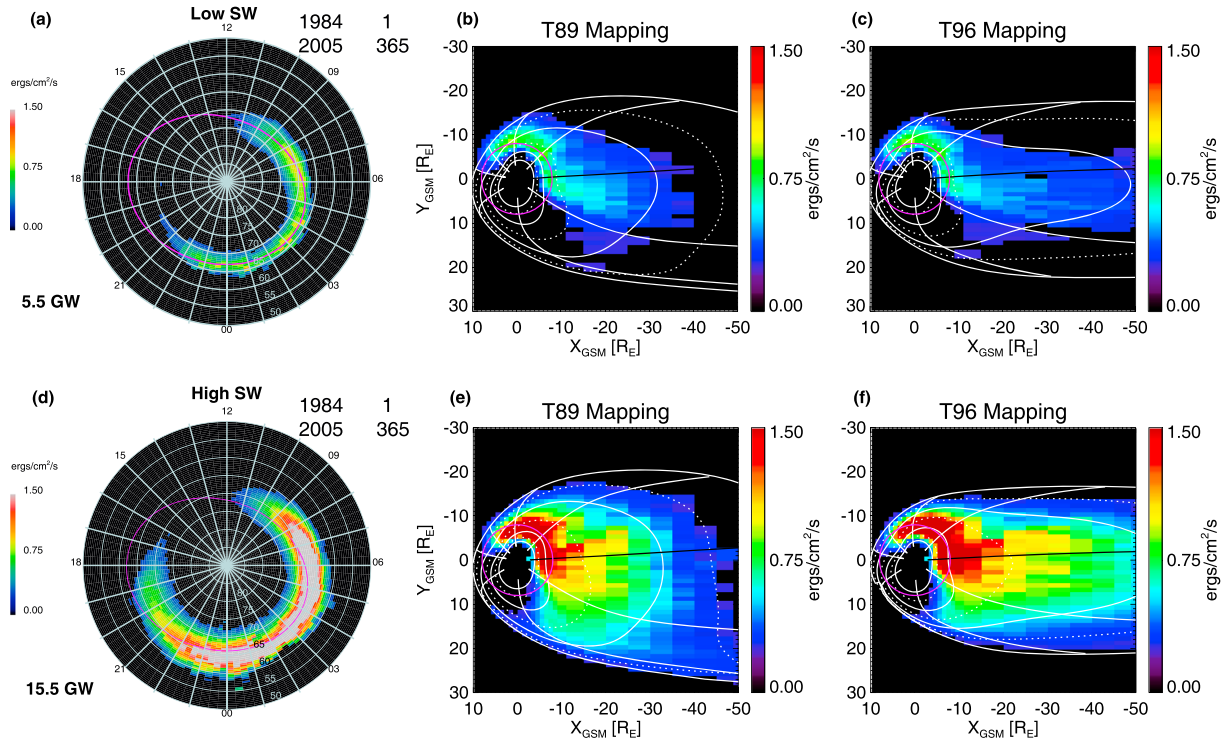

Figure 1. Electron diffuse auroral energy flux for (a) low and (b) high solar wind driving as a function of magnetic latitude (MLAT) and magnetic local time (MLT), obtained from OVATION Prime model. Only bins with energy fluxes greater than 0.25 ergs/cm^2/s are shown here and included in the subsequent analysis in order to eliminate low-amplitude noises. (b and c) Distributions of energy flux during low solar wind driving mapped to the equatorial plane using T89 and T96 magnetic model, respectively. (e and f) Distributions of energy flux during high solar wind driving mapped to the equatorial plane using T89 and T96 magnetic model, respectively. In Figures 1b, 1c, 1e, and 1f, white lines represent the MLT contours in the ionosphere every 3 h, with midnight marked by the overlaid black line; white solid circles denote the MLAT contours in the ionosphere at 60°, 65°, 70°, and 75°, while white dotted circles represent the MLAT contours in the ionosphere at 62.5°, 67.5°, and 72.5°. In Figures 1a and 1d, the magenta ovals mark the latitudes which map to equatorial radial distance of 8 R_E (denoted by the magenta circles in Figures 1b, 1c, 1e, and 1f) using the T89 magnetic field model.

It is clear that the diffuse auroral precipitation is most intense in the premidnight to dawn MLT sectors, following the drift path of injected plasma sheet electrons. Under low solar wind driving conditions, the total power due to electron precipitation into the ionosphere from the outer magnetosphere (defined as antisunward of the terminator and having equatorial radial distance greater than 8 R_E) is 1.25 GW for T89 (1.24 GW for T96). As shown in Figure 2, this corresponds to 58% of the total nightside precipitation (nightside was defined as negative X locations in the equator) in T89 (57% for T96). Although precipitation increases globally during high solar wind driving conditions, the above ratio decreases somewhat, to 42% for T89 mapping results and 55% for T96 results. This is partly due to an equatorward shift in the peak of diffuse auroral energy flux and partly due to a change in the auroral oval area subtended within the <8 R_E equatorial mapping region—a property of the mapping change during the more active conditions. Given that our choice of an 8 R_E geocentric distance to denote the boundary between inner and outer magnetosphere is somewhat arbitrary, the results suggest that a significant (~50%) portion of the precipitation is contributed by outer magnetosphere processes even during active times, whereas at quiet times the outer magnetosphere contribution is dominant.

3. Modeling ECH Wave Scattering of Plasma Sheet Electrons

In order to model diffusion due to wave-particle interactions between ECH waves and plasma sheet electrons throughout the nightside magnetosphere, we need to first determine the distribution of wave power, magnetic field magnitude and curvature (both relevant for loss cone size and ray propagation), and plasma parameters (density, temperature, and anisotropy, all relevant to local wave growth), which will be necessary for quantifying the scattering rates. Using the calculated diffusion coefficients of ECH waves at various equatorial locations, we then model the diffusion using quasi-linear theory, from which we infer the loss cone

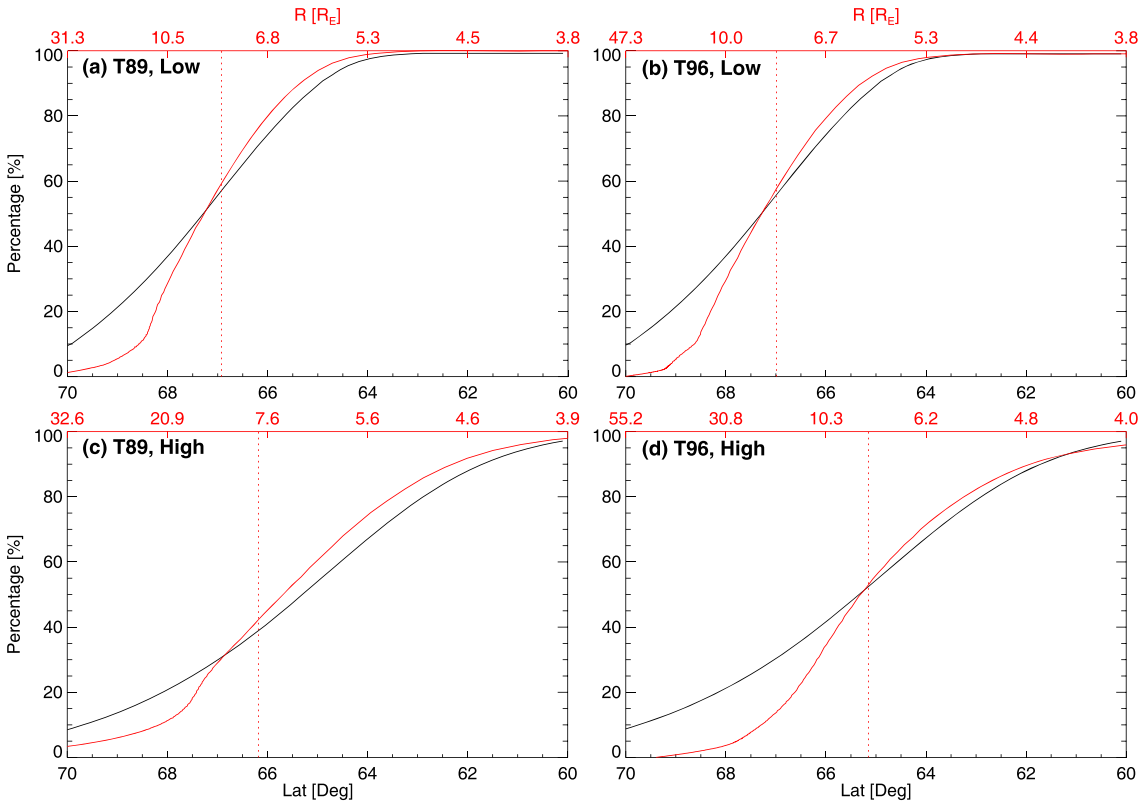

Figure 2. Cumulative percent contribution of diffuse auroral energy flux relative to total nightside precipitation, as a function of MLAT (black traces) and equatorial radial distance (red traces). (a and b) The result during low solar wind driving mapped to the equatorial plane using T89 and T96 magnetic model, respectively. (c and d) The same quantity during high solar wind driving mapped to the equatorial plane using T89 and T96 magnetic model, respectively. Red lines (and labels) show the corresponding equatorial radial distances for each latitude assuming at midnight MLT (mapping using the relevant magnetic field model). The red vertical dotted line marks the equatorial radial distance of 8 R_E.

filling ratio of electron distributions under the steady state. We shall use those to estimate the contribution of ECH waves to precipitation losses as a function of location and compare the results with OVATION estimates of diffuse auroral energy fluxes in section 4.

3.1. Spatial Distribution of ECH Waves

THEMIS comprises five identical spacecraft equipped with comprehensive particle and field instruments [*Angelopoulos*, 2008]. The Fluxgate Magnetometer (FGM) [*Auster et al*., 2008] measures background magnetic fields, which are used in this study to evaluate the local electron cyclotron frequencies. Electron distributions from a few eV up to 30 keV are recorded by the electrostatic analyzers (ESA) [*McFadden et al*., 2008]. Wave electric and magnetic fields in three orthogonal directions are collected by the Electric Field Instrument (EFI) [*Bonnell et al*., 2008] and Search Coil Magnetometer (SCM) [*LeContel et al*., 2008; *Roux et al*., 2008]. The Digital Fields Board [*Cully et al*., 2008] calculates the mean amplitude of the electric and magnetic fields in six logarithmically spaced frequency bands from ~2 Hz to 6 kHz (from EFI and SCM data), producing Filter Bank (FBK) data with a cadence of 4 s. FBK data are used in this study to select ECH wave emissions.

We use the same ECH wave database as developed by *Zhang et al*. [2014], which includes ECH emissions (represented by individual data samples within ECH events) in the plasma sheet (with plasma beta >0.5) captured by five THEMIS spacecraft during five tail science phases (in 2008–2012). ECH events are defined by *Zhang and Angelopoulos* [2014] as continuous intervals of wave activity (instantaneous wave amplitude >0.03 mV/m to exclude low-amplitude noise) with peak wave amplitudes >0.1 mV/m (refer to *Zhang and Angelopoulos* [2014, Figure 1] for an example). As shown by *Zhang et al*. [2014], the spatial distribution of the ECH occurrence rate in the XY plane (in aberrated GSM coordinates with a 4° aberration angle) has a slight dawnward preference within 10 R_E; outside of that distance, it is preferentially seen in the premidnight sector.

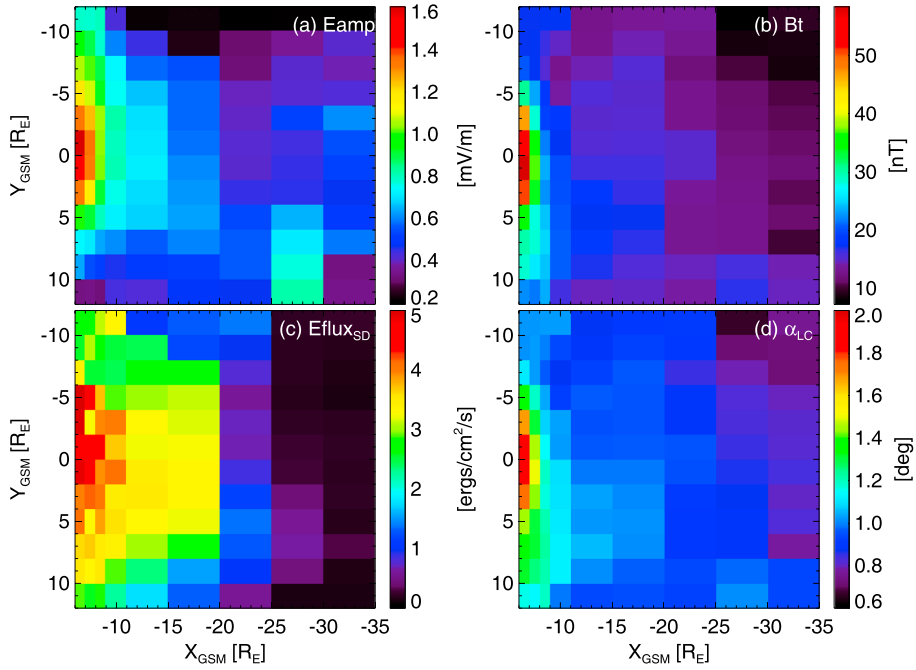

Figure 3. Distribution (during ECH events) of (a) average ECH wave amplitude, (b) median magnetic field magnitude, (c) energy flux during strong diffusion limit inferred from average magnetic field-aligned (pitch angle range 0°–22.5°) electron energy flux, $J_{//}$, within the energy range of 50 eV to 25 keV (energy range of ESA instrument excluding photoelectrons), and (d) loss cone size inferred from the magnetic field magnitude in panel (b).

This resembles the pattern of diffuse aurora shown in Figure 1. Despite the poor sampling of the regions beyond 15 R_E due to the THEMIS orbits (there have only been 2 years of traversals of that region by only two THEMIS probes), the low occurrence rates observed beyond 15 R_E (<10%) are statistically significant as evidenced by large scale averaging and are likely due to the small wave amplitudes expected at these distances. As discussed by *Zhang et al.* [2013], typical wave power can be below instrument sensitivity level there, more often than at lower distances, due to the smallness of the loss cone.

Plasma and magnetic field characteristics related to ECH waves are important for modeling the wave excitation, propagation and interaction with electrons. The distribution of wave power and relevant electron and magnetic field parameters during ECH emission intervals is shown in Figure 3.

Wave amplitude is the critical parameter in estimating the diffusion coefficients; it is a proxy for wave power and since it is recorded as the mean of the absolute value of the bandpass-filtered signal in the FBK data product, we multiply the raw FBK electric field value by a factor $\pi/2$ to convert it into the nominal wave amplitude [e.g., *Cully et al.*, 2008]. We determine the peak wave amplitude during each ECH event. As the plasma sheet flaps north-south (along the Z direction), and the neutral sheet is encountered occasionally, the ECH amplitude fluctuates due to spatial aliasing. To avoid this, we use the peak amplitude during each wave event as representative of the amplitude at the neutral sheet. We then take the average value of the peaks from all events within each (X, Y) spatial bin to construct the distribution of wave amplitudes throughout the equatorial magnetosphere. In order to reduce the data scattering due to limited data points beyond ~20 R_E, we further smooth the distribution by averaging over nine adjacent bins (3×3 bins in two dimensions, X and Y, appropriately weighted by the number of events within each bin) centered at the original bin. The total magnetic field magnitude (B_t) quantity is important, as it will be used to infer the local electron gyrofrequency and loss cone size. The field-aligned electron energy fluxes ($J_{//}$) are also important, as they are representative of the electron distribution just outside the loss cone that is relevant for precipitation; they will be used for quantifying the electron precipitation energy flux once the loss cone filling ratio has been evaluated. We use the average B_t and $J_{//}$ (during ECH emission intervals) within each bin to construct the distribution of these parameters. Similar to the wave amplitudes, we further smooth the B_t and $J_{//}$ distributions to reduce statistical noise by two dimensional averaging over nine adjacent bins.

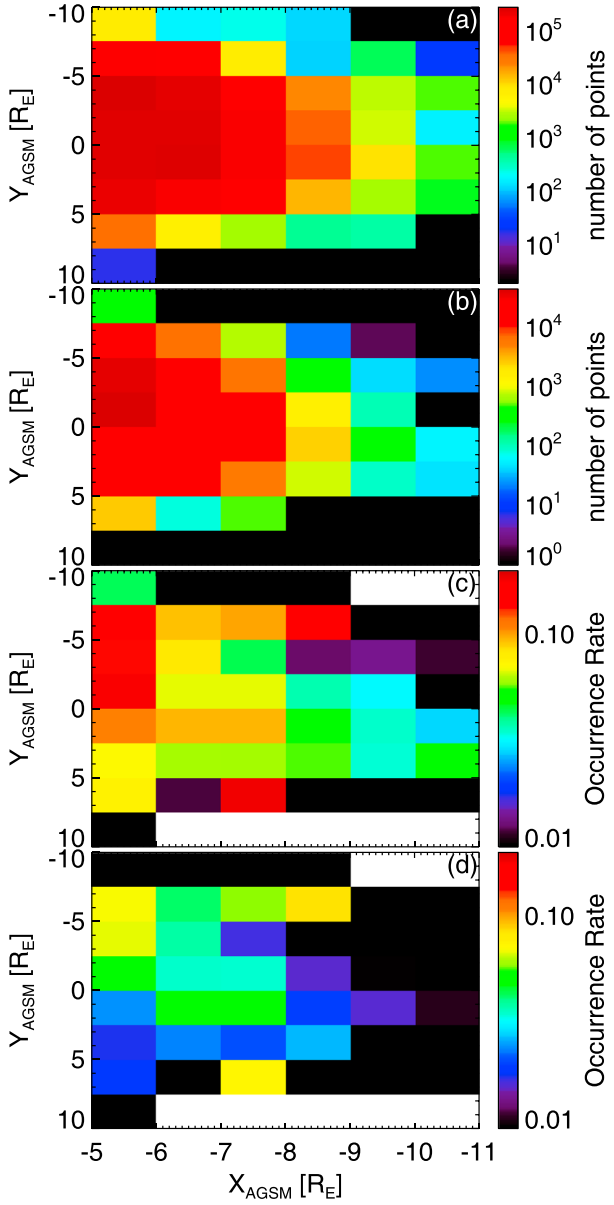

Figure 4. Distribution of (a) valid measurements (orbital distribution with valid SCM data) and (b) chorus observations from single spacecraft in the XY plane (in aberrated GSM coordinates). (c) Occurrence rate of chorus emissions computed as the ratio of Figures 4b to 4a. (d) Occurrence rate of chorus emissions with wave amplitudes >10 pT.

The average wave amplitude decreases with increasing distance down the tail; it is more intense near premidnight beyond X = −15 R_E, but near dawn earthward of X = −15 R_E (Figure 3a). The magnetic field magnitude shows a slight asymmetry across the midnight meridian (Figure 3b), with larger values at the dusk side, leading to a similar asymmetry for the distribution of loss cone size (Figure 3d). This is likely due to the increased presence of dipolarizing flux bundles (DFBs, i.e., the strong magnetic field region led by dipolarization fronts) and injections (known to preferentially occur in the premidnight sector [*Birn et al.*, 1997; *Gabrielse et al.*, 2014; *Liu et al.*, 2013]) in our database of ECH emissions, since ECH waves are correlated with these active time phenomena [*Zhang and Angelopoulos*, 2014]. The DFBs, which bring new magnetic flux from the tail, are expected to enhance the total magnetic field preferentially in the premidnight sector. The total energy flux in the strong diffusion limit also shows an asymmetry toward the dusk side (Figure 3c). This is predominantly due to higher occurrence rate of electron injections that enhance electron fluxes preferentially in the premidnight sector.

Since chorus waves are another potential contributor to diffuse auroral precipitation, we want to compare the occurrence rate distribution of chorus to that of ECH waves using the same (FBK) database of THEMIS plasma sheet crossings. Following *Li et al.* [2009], we select wave magnetic field data between 0.1 f_{ce} and 0.8 f_{ce} (i.e., typical frequency range of chorus) as chorus emissions. We estimate the electron cyclotron frequency (f_{ce}) from the local northward magnetic field component that approximates the equatorial magnetic field. Following *Li et al.* [2009], data with f_{ce} larger than 10 kHz (restricted by the maximum frequency of the FBK data) or smaller than 800 Hz (in order to eliminate chorus emissions that fall into the frequency bands below 80 Hz that are affected by conducted spacecraft emissions and cannot be cleaned without raw waveforms) are excluded from the analysis. The database thus only extends from $X = -5$ R_E to $X = -11$ R_E. We present in Figure 4 the spatial distribution of the chorus wave occurrence rates in the XY plane (in aberrated GSM coordinates with a 4° aberration angle). Compared to the distribution of ECH waves in the overlap region, the occurrence rate of moderate (wave amplitudes >10 pT) chorus emissions drops significantly (to <1%) beyond 8 R_E, indicating that chorus waves are statistically weak (a few pT) in the outer magnetosphere.

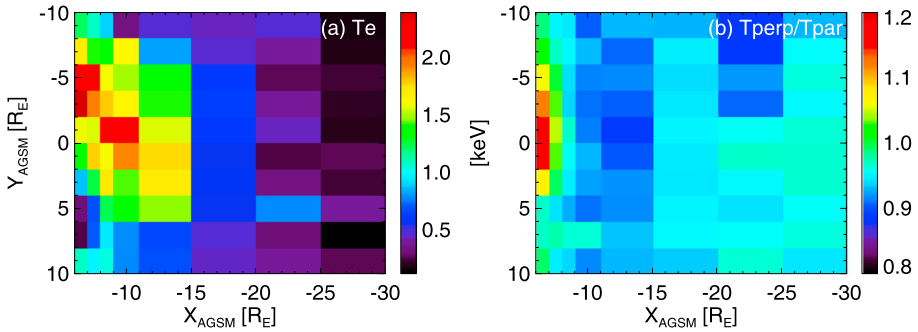

Figure 5. Distribution of (a) median electron temperature and (b) median temperature anisotropy ($T_\perp/T_{//}$) in the XY plane (in aberrated GSM coordinates). Data are collected within the central plasma sheet (with plasma beta >0.5).

Since chorus emissions may still be present beyond 8 R_E but with amplitudes below the detection threshold of the SCM instrument, we investigate other possible evidence of chorus using plasma data. Plasma temperature anisotropy is important in controlling the magnitude of chorus growth rates. We thus examine the distribution of temperature anisotropy in the central plasma sheet (characterized by plasma beta >0.5), where chorus waves are typically confined to. Electron temperature anisotropy here is denoted by the ratio of perpendicular to parallel (relative to the magnetic field) temperature from ESA measurements, i.e., $T_\perp/T_{//}$. As shown in Figure 5, $T_\perp/T_{//}$ is greater than 1 only within $X\sim -8\ R_E$, which can provide free energy for the excitation of the strong chorus emissions confined within the same region (Figure 4d), but not outside of that radius. This confirms that not only chorus amplitudes are low but also that the perpendicular electron anisotropies needed for chorus wave generation are virtually nonexistent in the outer magnetosphere.

3.2. Quantifying Diffusion Coefficients

In this section, we compute the ECH wave scattering rates assuming curvature and magnetic field intensity (scaled by f_{ce} from observations) conditions inferred from the T89 model, the same one we used for mapping the diffuse aurora to the neutral sheet in Figure 1. Estimation of local diffusion rates requires knowledge of the latitudinal confinement of ECH waves and the latitudinal variations of wave normal angle, wave number, and wave power, which are difficult to acquire directly from observations. Even at the equator, the (hot plasma) dispersion relation requires knowledge of the total-to-cold electron density ratio phase-space gradient near the loss cone and the temperature anisotropy of thermal electrons. With regards to the cold electron density, present instrumentation cannot measure low energy electron densities accurately enough due to the presence of photoelectrons (a few eV range) and backscattered electrons (occasionally up to tens of eV range) contaminating the measured distributions. Moreover, past and planned instruments are not equipped with angular resolution sufficient to measure the distribution function (or its velocity space gradients) within the loss cone. We thus infer the equatorial wave number from the resonant condition and the local electron gyrofrequency by assuming a minimum resonant energy of 500 eV (estimated by solving the hot plasma dispersion relation corresponding to an average temperature anisotropy during ECH intervals) for a fixed wave frequency. We used a wave frequency $f=1.5f_{ce}$ and a wave normal angle of 89.5° (based on the wave normal angle range that can lead to wave growth in the adopted hot plasma distribution) at the equator to represent the first harmonic. Since the observed ECH emissions are confined within a few degrees of the magnetic equator [e.g., *Belmont et al*., 1983; *Roeder and Koons*, 1989; *Meredith et al*., 2009; *Ni et al*., 2011c], the maximum latitude (λ_{max}) over which ECH waves exist is assumed to be varying over the nightside magnetosphere as shown in Figure 6, from 5.7° in the closest ($X=-6.5\ R_E$; $Y=1.0\ R_E$) bin to 0.7° in the farthest ($X=-32.5\ R_E$; $Y=11.0\ R_E$) bin. Following *Ni et al*. [2011a, 2012a], we linearly interpolate between the minimum magnetic field magnitude location and λ_{max} to obtain the latitudinal variation of wave normal angle (approaching 90° at λ_{max}), parallel wave number (assuming perpendicular wave number unchanged with latitudes), and the spread in parallel wave numbers.

Using the T89 magnetic field model, we then incorporate the aforementioned distributions of wave parameters and plasma properties into the diffusion rate formulas described by *Ni et al*. [2012b]. We thus estimate the bounce-averaged scattering rates for all equatorial nightside plasma sheet locations. Figure 7

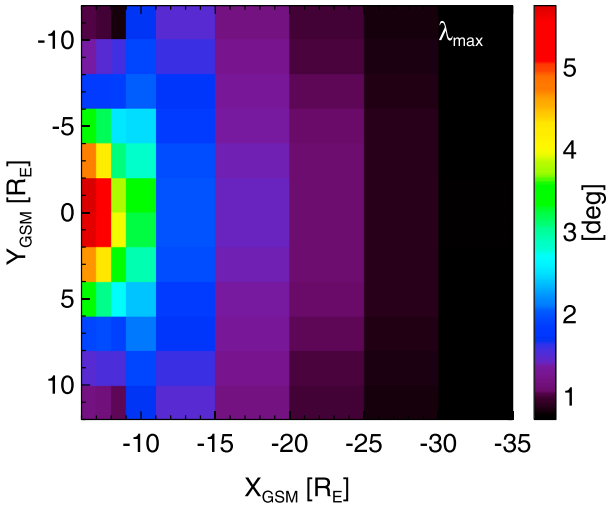

Figure 6. Distribution of latitudinal confinement of ECH waves in units of degrees.

shows results for two limiting cases near midnight: one closest to Earth ($X = -6.5\ R_E$, $Y = -1.0\ R_E$) and one furthest from Earth ($X = -32.5\ R_E$, $Y = -1.0\ R_E$). To investigate the efficacy of ECH waves in scattering plasma sheet electrons, we compare the pitch angle scattering rates at the edge of the loss cone $\langle D_{\alpha\alpha}\rangle|_{LC}$ with the strong diffusion rate D_{SD} defined by *Kennel* [1969] as

$$D_{SD} = \frac{2(\alpha_{LC})^2}{\tau_B} \quad (1)$$

where τ_B is the electron bounce period along the entire field line determined as [*Ni et al.*, 2012a, 2012b]

$$\tau_B = \frac{2}{v}\int_{\lambda_{m,s}}^{\lambda_{m,n}} \sec\alpha \sqrt{r^2 + \left(\frac{\partial r}{\partial \lambda}\right)^2}\, d\lambda \quad (2)$$

with v denoting the electron thermal speed, α for local pitch angle, r for radial distance from the Earth, λ for magnetic latitude, and $\lambda_{m,s}$ and $\lambda_{m,n}$ representing the mirror latitudes on the southern and northern hemisphere.

As shown in Figure 7, intense ECH wave scattering in the near-Earth plasma sheet occurs only for electrons with pitch angles $< 20°$ and over a limited energy range (0.2–1 keV), consistent with numerical results by *Thorne et al.* [2010], *Tao et al.* [2011], and *Zhang et al.* [2013]. Compared to pitch angle diffusion rates, momentum diffusion rates and mixed diffusion rates (not shown here) by ECH waves are small both near the Earth and in the distant tail plasma sheet, suggesting that ECH emissions play only a minor role in energizing plasma sheet electrons. It is also clear, however, that at larger distances ECH waves tend to efficiently scatter progressively larger pitch angle and lower energy (<200 eV) electrons. This is due to increased magnetic field line stretching with distance from Earth. Moreover, as seen in Figures 7c and 7f, the strong diffusion rate D_{SD} decreases by at least one order of magnitude from $X = -6.5\ R_E$ to $X = -32.5\ R_E$, due to smaller loss cone size and the more stretched (and thus longer) field lines at larger distances. Therefore, the domain of significant diffusion due to ECH waves expands to both progressively lower energies (due to the wave scattering in a progressively stretched field topology) and higher energies (because wave scattering rate approaches the strong diffusion rate D_{SD}), going from ~0.2–1 keV at $X = -6.5\ R_E$ to ~0.1–3 keV at $X = -32.5\ R_E$. This leads to efficient pitch angle scattering of both lower and (most importantly for powering the aurora) higher energy electrons in the outer magnetosphere.

3.3. Modeling Electron Diffusion Using Quasi-Linear Theory

Using the resonant scattering rates quantified above, we now model the evolution of the electron pitch angle distribution by its interaction with ECH waves using the 2-D bounce-averaged Fokker-Planck equation (equation (3)), to estimate the loss cone filling ratio at various locations throughout the nightside magneosphere

$$\frac{\partial f}{\partial t} = \frac{1}{S_0 \sin\alpha_{eq}\cos\alpha_{eq}}\frac{\partial}{\partial \alpha_{eq}}\left(S_0 \sin\alpha_{eq}\cos\alpha_{eq}\langle D_{\alpha\alpha}\rangle\frac{\partial f}{\partial \alpha_{eq}}\right) + \frac{1}{p^2}\frac{\partial}{\partial p}\left(p^2\langle D_{pp}\rangle\frac{\partial f}{\partial p}\right) - \frac{f}{\tau}. \quad (3)$$

Here p is the particle momentum, α_{eq} is the equatorial pitch angle, S_0 is the bounce period-related term, and $\langle D_{\alpha\alpha}\rangle$ and $\langle D_{pp}\rangle$ are the bounce-averaged pitch angle and momentum diffusion coefficients, respectively. Mixed diffusion terms $D_{\alpha p}$ were omitted in this equation. The loss time τ is set to one quarter of the bounce period (τ_B) if α_{eq} is less than the local loss cone angle α_{LC} and infinity otherwise. Our neglect of mixed diffusion

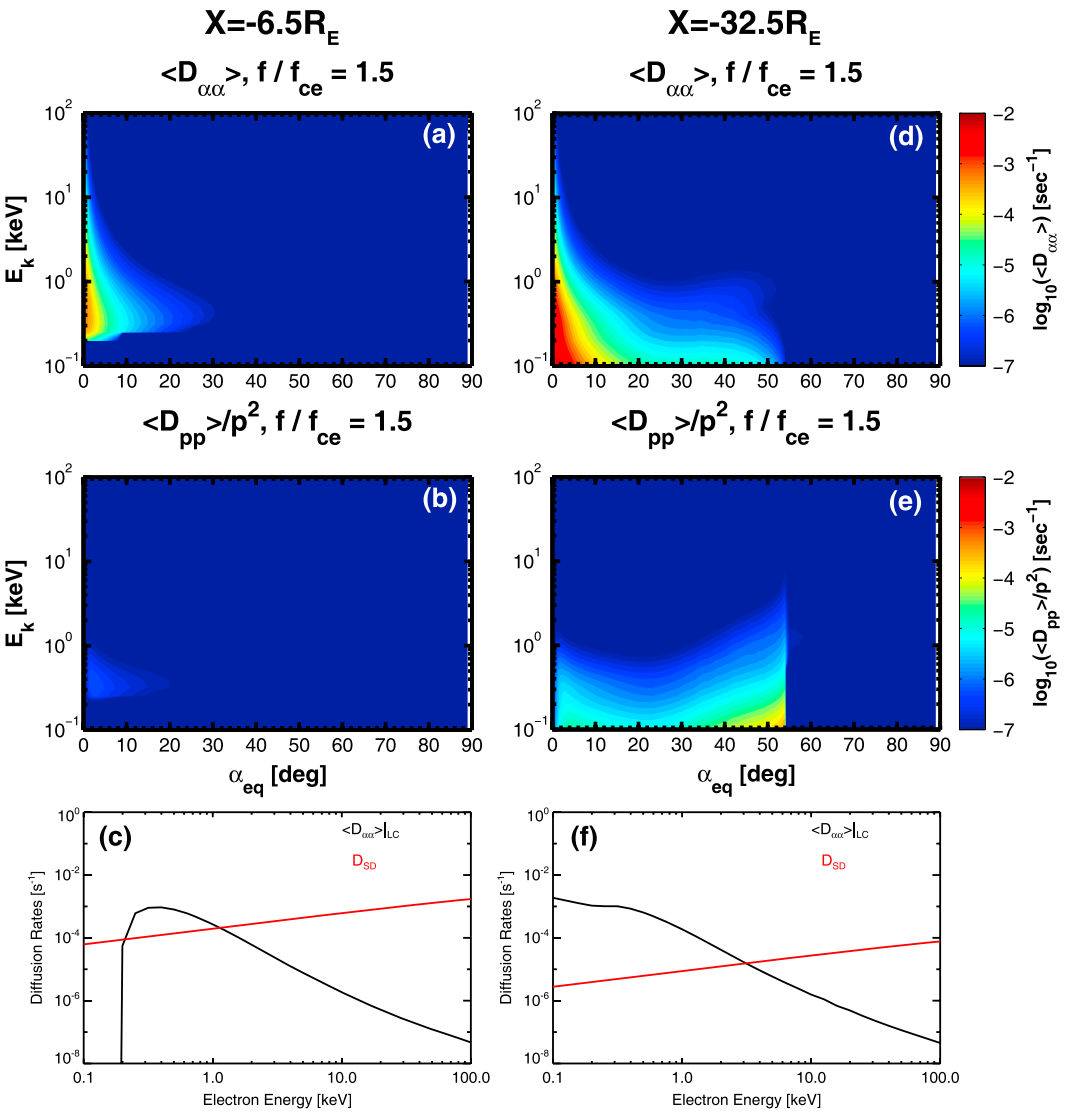

Figure 7. (a and d) Bounce-averaged pitch angle and (b and e) momentum diffusion coefficients as a function of equatorial pitch angle and electron kinetic energy due to ECH waves. (c and f) Comparison of pitch angle diffusion coefficients at the equatorial loss cone edge $\langle D_{\alpha\alpha}\rangle|_{LC}$ with strong diffusion rate D_{SD}. (a–c) The result at $X = -6.5\ R_E$, $Y = -1.0\ R_E$; (d–f) the result at $X = -32.5\ R_E$, $Y = -1.0\ R_E$.

terms simplifies the algorithm and reduces the computation time, while retaining the dominant diffusion process that affects plasma sheet electrons [e.g., *Albert and Young*, 2005].

The magnetic field-related parameters (S_0 andτ) in equation (3) are numerically evaluated for the T89 magnetic field following *Ni et al.* [2012a]. Since we compute the loss cone filling ratio from the resultant electron distributions, the absolute PSD values do not affect our modeling—we are interested in changes inside the loss cone relative to the PSD value outside. Generic initial conditions are therefore adopted from THEMIS observations, after suppressing anisotropies of the hot component outside the loss cone. Boundary conditions are the same as used in *Zhang et al.* [2013]: $\partial f/\partial\alpha_{eq} = 0$ at $\alpha_{eq} = 0^\circ$ and at $\alpha_{eq} = 90^\circ$ for the pitch angle operator. As shown in Figure 7, pitch angle diffusion rates may exceed the strong diffusion limit; we thus use the zero gradient condition at the low pitch angle boundary (applicable to both weak and strong diffusions) in this study. For the energy diffusion operator, the lower boundary is held constant at 55 eV because these low energy electrons do not contribute much to the precipitating energy flux (tested by our modeling results) and ESA measurements at these low energy channels are often contaminated by

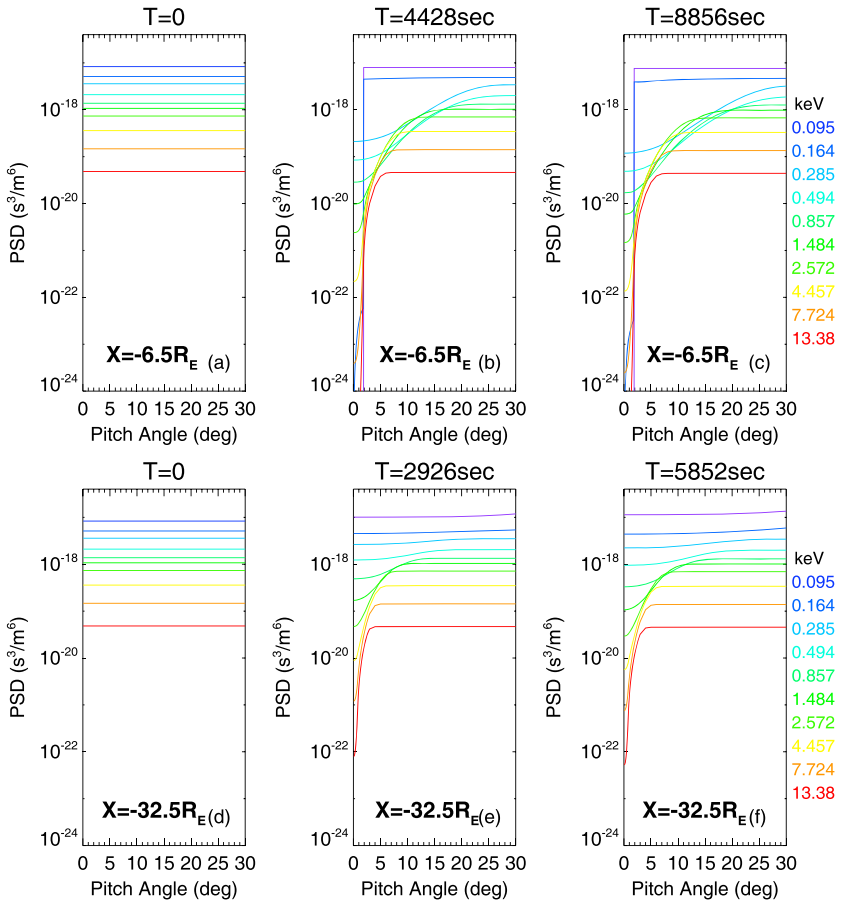

Figure 8. Initial electron distribution (isotropic) for modeling the diffusion process and the evolution of electron distribution after interaction with ECH waves at two time instants, with the last one (c and f) showing the distribution at the steady state. (a–c) The results at $X = -6.5\ R_E$, $Y = -1.0\ R_E$; (d–f) the results at $X = -32.5\ R_E$, $Y = -1.0\ R_E$.

photoelectrons; the upper boundary is also fixed at 23 keV, well above the typical resonant energies of ECH waves with plasma sheet electrons (hundreds of eV to several keV).

Figure 8 shows modeled results for the evolution of electron distributions at $X = -6.5\ R_E$, $Y = -1.0\ R_E$ and $X = -32.5\ R_E$, $Y = -1.0\ R_E$. We assume that the steady state has been reached when the electron PSD over potentially resonant energies (100 eV to 5 keV) changes less than 1% in one time step (2 s); the electron distributions for that state are shown in Figures 6c and 6f. The loss cone filling ratio is then estimated using the median value of resultant PSD within the loss cone divided by that at the edge of the loss cone.

4. Estimated Precipitation due to ECH Wave Scattering

Assuming isotropic differential energy flux within a loss cone, the ionospheric precipitation from ECH wave scattering plasma sheet electrons can be estimated by [*Liang et al.*, 2011; *Ni et al.*, 2012a]

$$\Phi = \pi \int_{E_1}^{E_2} \chi_{(E)} J_{(E,\alpha_{LC})} dE \tag{4}$$

where Φ is the energy flux into the ionosphere, $\chi_{(E)}$ is the loss cone filling ratio estimated above by modeling the electron distribution at the steady state, $J_{(E,\alpha_{LC})}$ is the electron differential energy flux near the equatorial loss cone approximated by the field-aligned energy flux from THEMIS ESA measurements, and dE is the width of each energy channel.

The electron differential energy fluxes within the equatorial loss cone using the estimated filling ratios are shown in Figure 9 for the two cases discussed in Figures 6 and 7. $\chi_{(E)}$ is 1 for electrons with pitch angle scattering rate exceeding the strong diffusion rate, but it drops dramatically for other energies with lower

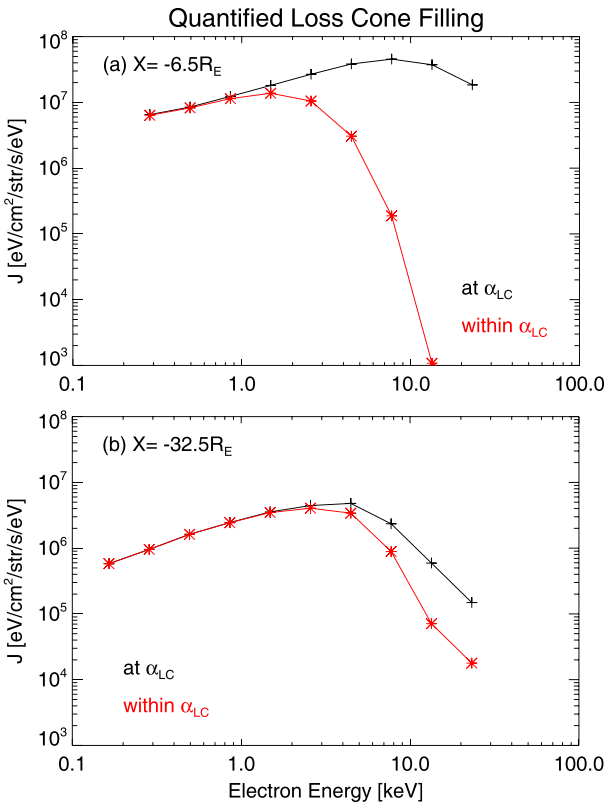

Figure 9. Electron differential energy flux at the equatorial loss cone (black curve) approximated by the field-aligned energy flux from THEMIS ESA measurements, compared with the differential energy flux within the loss cone (red curve) estimated using the loss cone filling ratio due to ECH wave scattering. (a) The result at $X = -6.5\ R_E$, $Y = -1.0\ R_E$; (b) the result at $X = -32.5\ R_E$, $Y = -1.0\ R_E$.

diffusion rates than the strong diffusion limit. It is evident by comparing Figures 8a and 8b that ECH waves can fill in the loss cone more efficiently at $X = -32.5\ R_E$, $Y = -1.0\ R_E$, especially for electrons at higher energies (>2 keV).

By summing up the electron energy flux inside the loss cone (following equation (4)), we estimate electron precipitation caused by ECH wave scattering in Figure 10. The ECH wave-induced electron precipitation is predominantly in the dusk sector at larger distances (beyond 20 R_E) and becomes more intense in the dawn sector closer to the Earth (within 20 R_E), which agrees well with diffuse auroral precipitation (OVATION Prime model result) mapped from the ionosphere (Figure 10a). For consistency, we model the diffuse aurora using the median solar wind driving parameter (defined by *Newell et al.* [2007]) in the ECH wave database. ECH wave-induced precipitation contributes at most 40% of the total energy flux associated with the diffuse aurora in the inner magnetosphere ($X = -6.5\ R_E$, $|Y| \leq 3\ R_E$). However, the ECH wave-contributed energy flux becomes closer to 100% of the anticipated energy flux in the diffuse aurora in the outer magnetosphere (within 20 R_E). Beyond 25 R_E, although the loss cone filling ratio is high, the estimated precipitation is inadequate to account for the expected diffuse auroral ionospheric power due to the low electron temperature (and field-aligned energy flux) in the plasma sheet at those distances.

Finally, we map the results back into the ionosphere to illustrate ECH wave contributions at different magnetic latitudes (MLATs). As shown in Figure 11, wave-induced precipitation resembles the diffuse auroral pattern in the overlap regions, especially at MLAT between ~67° and ~70°. In addition, these ECH wave-induced precipitations constitute the majority of the diffuse auroral energy fluxes for MLATs greater than ~67° (Figure 11c), which maps to beyond ~8 R_E in the magnetosphere. Consistent with the result mapped in the magnetotail (Figure 10b), ECH wave contribution beyond ~69° is smaller due to insufficient electron energy fluxes in the plasma sheet (as illustrated by Figures 2c and 9a).

5. Summary and Discussion

We modeled the diffuse auroral precipitation using the OVATION Prime model [*Newell et al.*, 2009, 2010] and mapped the energy flux to the magnetic equator using T89 and T96 magnetic field models. We adopted appropriate parameters to represent low (lower quartile of the same database) and high (upper quartile of the same database) solar wind driving conditions separately for T89 and T96 models. We found that during low solar wind driving conditions (Figure 2), ~60% of the nightside diffuse aurora is contributed by precipitations from the outer magnetosphere ($R > 8\ R_E$). For high solar wind driving, precipitation from these high L shells accounts for 42–55% of the entire nightside energy fluxes. This is in agreement with the finding of *Petrinec et al.* [1999], who showed that during active times the diffuse aurora intensifies and extends to low latitudes, and therefore, the relative contribution of high-latitudes to the total diffuse auroral precipitation decreases. This decrease is probably due to the intensified whistler-mode chorus emissions during higher

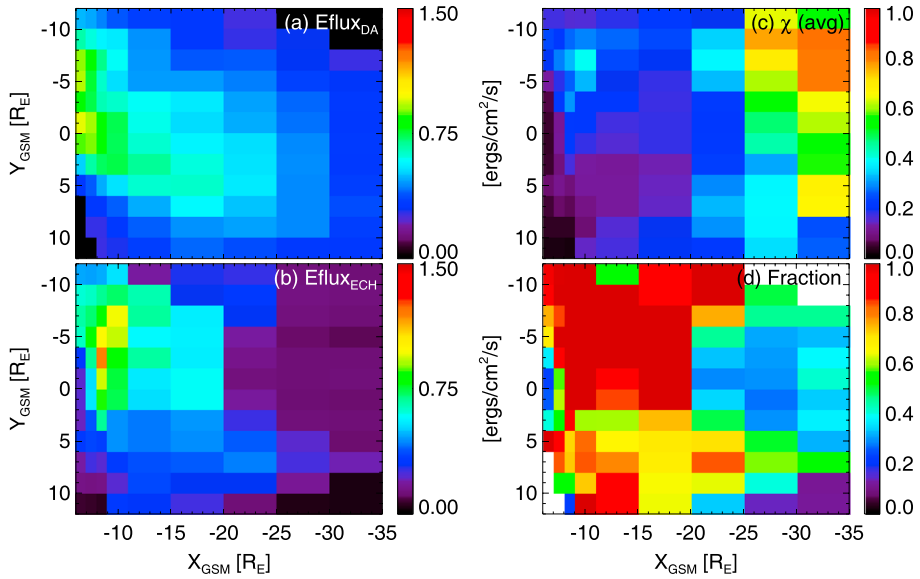

Figure 10. Distribution of (a) ionospheric diffuse auroral precipitation energy flux (OVATION Prime model) mapped to the magnetic equator (using T89 magnetic field model) under median solar wind driving condition during the ECH wave measurement intervals, (b) ECH wave-induced electron precipitation, (c) loss cone filling ratio computed as the ECH wave-induced precipitating energy flux divided by that at the strong diffusion limit, and (d) fraction of diffuse auroral precipitation contributed by ECH wave scattering.

geomagnetic activity levels in the inner magnetosphere. We note that T89 and T96 have been shown to be overstretched in the outer magnetosphere during active times, while T89 is understretched during quiet times [*Huang et al.*, 2008; *McCollough et al.*, 2008; *Yue et al.*, 2013]. Therefore, the contribution of the outer magnetosphere ($R > 8\ R_E$) to the entire nightside diffuse aurora may be underestimated during low solar wind driving but is likely overestimated during high solar wind driving. This further supports our argument that the relative contribution of ECH waves to the diffuse aurora from the outer magnetosphere is likely dominant during quiet times.

In order to further explore the origin of high L shell precipitation, we also investigated the occurrence rate distribution of chorus emissions and compared it with that of ECH waves. Consistent with the previous study [*Li et al.*, 2009], we found that chorus emissions are weak (a few pT) and rare outside of $X = -8\ R_E$ (Figure 4) and thus would not be able to contribute significantly toward plasma sheet electron scattering there. We further examined the distribution of plasma parameters relevant to the generation of chorus waves. Our results indicate that the conditions for chorus generation (enhanced perpendicular electron temperature anisotropy) only exist at $X > -8\ R_E$ (Figure 5b), consistent with the preferred location of intense chorus emissions. These observations agree with previous investigations on chorus generation [*Li et al.*, 2010]. In particular, enhanced temperature anisotropy can provide free energy for the excitation of upper band chorus (resonating with electrons at energies between 500 eV and a few keV). As shown in Figure 5b, absence of such a free energy source beyond ~8 R_E further indicates chorus waves cannot exist outside of the inner magnetosphere. However, moderately strong ECH waves (wave amplitude >0.1 mV/m) can still be observed even beyond $X = -20\ R_E$, indicating that ECH waves can potentially be a significant driver of high-latitude diffuse aurora.

We then numerically modeled the interaction between plasma sheet electrons and ECH waves to estimate the loss cone filling ratio and the corresponding electron precipitation due to ECH wave scattering. To quantify the diffusion coefficients, we first obtained the distribution of wave amplitude and magnetic field magnitude (adjusting the electron cyclotron frequency and the loss cone size in the model based on the average magnetic field value during our observations) statistically from THEMIS ECH wave database, as presented in Figure 3. After block-averaging, we obtained realistic but smoothly varying spatial distributions of wave amplitude, magnetic field magnitude, and temperature for use in further modeling of ECH wave growth, propagation and estimation of the diffusion coefficients. To eliminate variations in the wave number

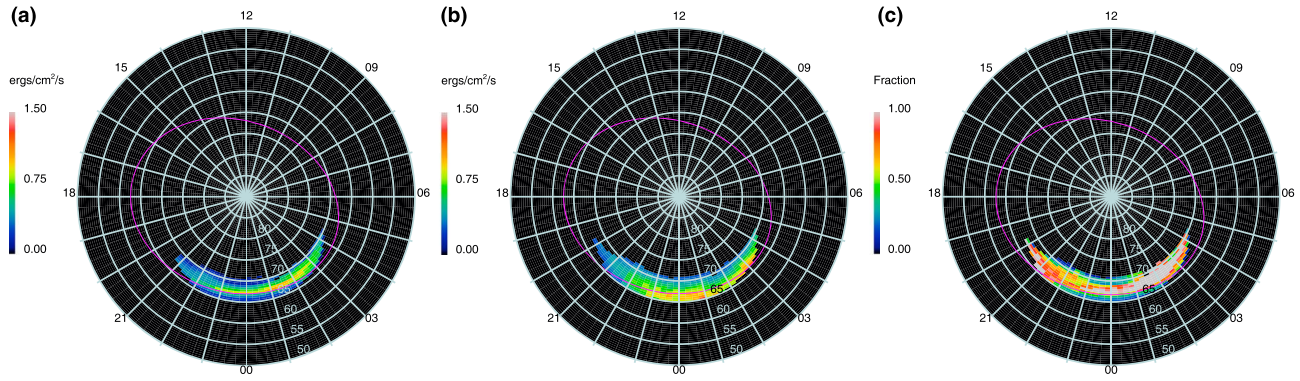

Figure 11. Ionospheric distribution of (a) ECH wave-induced electron precipitation energy flux (obtained by mapping the result in Figure 10b to the ionosphere using T89 magnetic field model), (b) diffuse auroral precipitation from OVATION Prime model under median solar wind driving condition during ECH wave measurement intervals (only regions with wave measurements are shown, in order to better compare with Figure 11a), and (c) fraction of diffuse auroral precipitation contributed by ECH wave scattering (determined by the ratio of data in Figure 11a over Figure 11b). The magenta ovals mark the latitudes which map to equatorial radial distance of 8 R_E in T89 magnetic field model.

due to statistical fluctuations of plasma parameters from one equatorial location to another, we fixed the minimum resonant energy (500 eV) at each location and used a constant wave normal angle (89.5°) at the equator, both of which are typical values for ECH waves. For the wave latitudinal extent, which cannot be inferred from observations, we made reasonable estimates preserving the trend of progressive latitudinal confinement with increasing distance from the Earth, due to increased field line curvature. We intentionally adopted the same latitudinal confinement (at $X=-12.5\ R_E$, $Y=-1\ R_E$) as used in the case study by *Ni et al.* [2012a] at $L=11.5$ in order to cross-check and compare our results with theirs. Their (active plasma sheet) pitch angle diffusion coefficients are about 4 times larger than our (average, and thus preferentially inactive plasma sheet) results at all energies, primarily due to the factor of 2 smaller wave amplitude adopted in our study. This indicates that our single frequency approximation compares well with their multiple frequency (intensity-weighted) diffusion coefficients, and can thus feasibly represent the actual wave-particle interactions. Our numerically estimated loss cone filling ratio also agrees well with the analytical solution used by *Ni et al.* [2012a] under steady state condition: both studies obtain a filling ratio close to 1 for electrons with energy <1.5 keV (the transition from the domain of significant diffusion to moderate diffusion). But at higher energies, the smaller scattering rates in our study lead to much lower loss cone filling ratios, as expected.

Due to the decrease in loss cone size and increase in field line stretching, the strong diffusion rate decreases with increasing distance from the Earth, leading to more efficient scattering of plasma sheet electrons and high loss cone filling ratios in the outer magnetosphere. Using these loss cone filling ratios obtained from modeling electron diffusion, we were able to quantify the precipitation by integrating the field-aligned electron energy fluxes over resonant energies encompassing the field-aligned direction, assuming that they represent the fluxes at the edge of the loss cone. The ECH wave-induced precipitation (Figure 10b) occurs predominantly at premidnight beyond 20 R_E and migrates toward the dawn side in the inner magnetosphere, which resembles the modeled pattern of the diffuse aurora (Figure 10a). As shown in Figure 3c, there is a slight duskward preference in the electron energy flux distribution within ~10 R_E; thus, the dawnward preference of wave-induced precipitation at this region mainly results from larger wave amplitude and smaller loss cone size in the dawn sector (Figures 2a and 2d), corresponding to enhanced scattering from ECH waves. Electron energy fluxes beyond 25 R_E cannot account for the diffuse aurora even at strong diffusion limit, leading to the small contributions of ECH wave-induced precipitations (Figure 10d). This discrepancy is possibly related to the fact that at such high latitudes, *Newell et al.* [2009, 2010] may have inadvertently included discrete aurora in their diffuse auroral bins, due to their strict criteria in categorizing discrete aurora.

As far as we know, our study is the first attempt to quantitatively evaluate the contribution of ECH waves to diffuse auroral precipitation throughout the nightside magnetosphere. By numerically modeling the ECH wave-induced electron precipitation and evaluating the contribution relative to the diffuse auroral energy flux modeled at the ionosphere, we were capable of quantifying the role of ECH waves in driving the diffuse

aurora globally and directly. Adopting quasi-linear theory and a realistic nondipolar magnetic field topology on the basis of OVATION Prime model, we concluded that ECH waves are the major contribution to the diffuse aurora in the outer magnetosphere ($R > 8\ R_E$), while whistler-mode chorus is more likely the dominant driver of low-latitude diffuse electron precipitations, as previously discussed by *Thorne et al.* [2010] and *Ni et al.* [2011b].

Compared to earlier studies of the diffuse aurora, the OVATION Prime model is the first attempt to discriminate diffuse aurora from other forms of precipitation in a statistical fashion, and hence was used here to better depict the diffuse aurora equatorial source distribution in our study. In order to compare with ECH wave scattering effects, we modeled the diffuse auroral energy fluxes under the median solar wind driving conditions in our ECH wave database. Due to the relatively low solar activity levels during intervals of the ECH wave database (2008–2012 for regions of $X > -12\ R_E$; 2008–2009 for $X < -12\ R_E$), our conclusion that ECH waves dominate in the production of the diffuse aurora is, strictly speaking, representative of quiet geomagnetic times. However, given the absence of chorus wave emissions and a free energy source for them in the outer magnetosphere ($R > 8\ R_E$) at all times [*Li et al.*, 2010], we expect ECH waves to be an important driver of the diffuse aurora at higher latitudes during active times as well. Quantitative evaluations of ECH wave-induced precipitation relative to the entire diffuse aurora under various geomagnetic activity levels (with consistently defined indices at both low and high latitudes) are left for future detailed investigations.

Acknowledgments

We thank P. Newell for useful discussions and J. Hohl for her help with editing. We acknowledge NASA contract NAS5-02099 for use of data from the THEMIS Mission, NASA grants NNX12AD12G and NNX14AI18G. B. Ni also acknowledges the support from the NSFC grants 41204120 and 41474141 and from the Fundamental Research Funds for the Central Universities grant 2042014kf0251. We thank P. Newell and NOAA for use of OVATION Prime model; J. H. King and N. Papatashvilli at AdnetSystems, NASA GSFC and CDAWeb for use of OMNI data; J. W. Bonnell and F. S. Mozer for use of EFI data; D. Larson and R. P. Lin for use of SST data; C. W. Carlson and J. P. McFadden for use of ESA data; A. Roux and O. LeContel for use of SCM data; K. H. Glassmeier, and U. Auster and W. Baumjohann for the use of FGM data provided under the lead of the Technical University of Braunschweig and with financial support through the German Ministry for Economy and Technology and the German Center for Aviation and Space (DLR) under contract 50 OC 0302.

Michael Balikhin thanks the reviewers for their assistance in evaluating the paper.

References

Albert, J. M., and S. L. Young (2005), Multidimensional quasi-linear diffusion of radiation belt electrons, *Geophys. Res. Lett.*, *32*, L14110, doi:10.1029/2005GL023191.

Anderson, R. R., and K. Maeda (1977), VLF emissions associated with enhanced magnetospheric electrons, *J. Geophys. Res.*, *82*(1), 135–146.

Angelopoulos, V. (2008), The THEMIS Mission, *Space Sci. Rev.*, *141*, 5–34.

Auster, H. U., et al. (2008), The THEMIS fluxgate magnetometer, *Space Sci. Rev.*, *141*, 235–264, doi:10.1007/s11214-008-9365-9.

Belmont, G., D. Fontaine, and P. Canu (1983), Are equatorial electron cyclotron waves responsible for diffuse auroral electron precipitation?, *J. Geophys. Res.*, *88*(A11), 9163–9170, doi:10.1029/JA088iA11p09163.

Birn, J., M. F. Thomsen, J. E. Borovsky, G. D. Reeves, D. J. McComas, and R. Belian (1997), Characteristic plasma properties during dispersionless substorm injections at geosynchronous orbit, *J. Geophys. Res.*, *102*(A2), 2309–2324, doi:10.1029/96JA02870.

Bonnell, J. W., F. S. Mozer, G. T. Delory, A. J. Hull, R. Abiad, R. E. Ergun, C. M. Cully, V. Angelopoulos, and P. R. Harvey (2008), The Electric Field Instrument (EFI) for THEMIS, *Space Sci. Rev.*, *141*, 303–341, doi:10.1007/s11214-008-9469-2.

Cully, C. M., R. E. Ergun, K. Stevens, A. Nammari, and J. Westfall (2008), The THEMIS digital fields board, *Space Sci. Rev.*, *141*(1–4), 343–355, doi:10.1007/s11214-008-9417-1.

Fontaine, D., and M. Blanc (1983), A theoretical approach to the morphology and the dynamics of diffuse auroral zones, *J. Geophys. Res.*, *88*(A9), 7171–7184.

Gabrielse, C., V. Angelopoulos, A. Runov, and D. L. Turner (2014), Statistical characteristics of particle injections throughout the equatorial magnetotail, *J. Geophys. Res. Space Physics*, *119*, 2512–2535, doi:10.1002/2013JA019638.

Hardy, D. A., M. S. Gussenhoven, and E. Holeman (1985), A statistical model of auroral electron precipitation, *J. Geophys. Res.*, *90*(A5), 4229–4248, doi:10.1029/JA090iA05p04229.

Hardy, D. A., M. S. Gussenhoven, and D. Brautigam (1989), A statistical model of auroral ion precipitation, *J. Geophys. Res.*, *94*(A1), 370–392, doi:10.1029/JA094iA01p00370.

Horne, R. B., and R. M. Thorne (2000), Electron pitch angle diffusion by electrostatic electron cyclotron harmonic waves: The origin of pancake distributions, *J. Geophys. Res.*, *105*(A3), 5391–5402.

Horne, R. B., R. M. Thorne, N. P. Meredith, and R. R. Anderson (2003), Diffuse auroral electron scattering by electron cyclotron harmonic and whistler mode waves during an isolated substorm, *J. Geophys. Res.*, *108*(A7), 1290, doi:10.1029/2002JA009736.

Huang, C.-L., H. E. Spence, H. J. Singer, and N. A. Tsyganenko (2008), A quantitative assessment of empirical magnetic field models at geosynchronous orbit during magnetic storms, *J. Geophys. Res.*, *113*, A04208, doi:10.1029/2007JA012623.

Kennel, C., F. Scarf, R. Fredricks, J. McGehee, and F. Coroniti (1970), VLF electric field observations in the magnetosphere, *J. Geophys. Res.*, *75*(31), 6136–6152.

Kennel, C. F. (1969), Consequences of a magnetospheric plasma, *Rev. Geophys.*, *7*(1–2), 379–419.

Kurita, S., Y. Miyoshi, C. M. Cully, V. Angelopoulos, O. LeContel, M. Hikishima, and H. Misawa (2014), Observational evidence of electron pitch angle scattering driven by ECH waves, *Geophys. Res. Lett.*, *41*, 8076–8080, doi:10.1002/2014GL061927.

LeContel, O., et al. (2008), First results of the THEMIS searchcoil magnetometers, *Space Sci. Rev.*, (1–4), 509–534, doi:10.1007/s11214-008-9371-y.

Li, W., R. M. Thorne, V. Angelopoulos, J. Bortnik, C. M. Cully, B. Ni, O. LeContel, A. Roux, U. Auster, and W. Magnes (2009), Global distribution of whistler-mode chorus waves observed on the THEMIS spacecraft, *Geophys. Res. Lett.*, *36*, L09104, doi:10.1029/2009GL037595.

Li, W., et al. (2010), THEMIS analysis of observed equatorial electron distributions responsible for the chorus excitation, *J. Geophys. Res.*, *115*, A00F11, doi:10.1029/2009JA014845.

Liang, J., B. Ni, E. Spanswick, M. Kubyshkina, E. F. Donovan, V. M. Uritsky, R. M. Thorne, and V. Angelopoulos (2011), Fast earthward flows, electron cyclotron harmonic waves, and diffuse auroras: Conjunctive observations and a synthesized scenario, *J. Geophys. Res.*, *116*, A12220, doi:10.1029/2011JA017094.

Liu, J., V. Angelopoulos, A. Runov, and X.-Z. Zhou (2013), On the current sheets surrounding dipolarizing flux bundles in the magnetotail: The case for wedgelets, *J. Geophys. Res. Space Physics*, *118*, 2000–2020, doi:10.1002/jgra.50092.

Lyons, L. (1974), Electron diffusion driven by magnetospheric electrostatic waves, *J. Geophys. Res.*, *79*(4), 575–580.

McCollough, J. P., J. L. Gannon, D. N. Baker, and M. Gehmeyr (2008), A statistical comparison of commonly used external magnetic field models, *Space Weather*, *6*, S10001, doi:10.1029/2008SW000391.

McFadden, J. P., C. W. Carlson, D. Larson, M. Ludlam, R. Abiad, B. Elliott, P. Turin, M. Marckwordt, and V. Angelopoulos (2008), The THEMIS ESA plasma instrument and in-flight calibration, *Space Sci. Rev.*, *141*, 277–302, doi:10.1007/s11214-008-9440-2.

Meredith, N. P., R. B. Horne, A. D. Johnstone, and R. R. Anderson (2000), The temporal evolution of electron distributions and associated wave activity following substorm injections in the inner magnetosphere, *J. Geophys. Res.*, *105*(A6), 12,907–12,917, doi:10.1029/2000JA900010.

Meredith, N. P., R. B. Horne, R. M. Thorne, and R. R. Anderson (2009), Survey of upper band chorus and ECH waves: Implications for the diffuse aurora, *J. Geophys. Res.*, *114*, A07218, doi:10.1029/2009JA014230.

Newell, P. T., T. Sotirelis, K. Liou, C.-I. Meng, and F. J. Rich (2007), A nearly universal solar wind-magnetosphere coupling function inferred from 10 magnetospheric state variables, *J. Geophys. Res.*, *112*, A01206, doi:10.1029/2006JA012015.

Newell, P. T., T. Sotirelis, and S. Wing (2009), Diffuse, monoenergetic, and broadband aurora: The global precipitation budget, *J. Geophys. Res.*, *114*, A09207, doi:10.1029/2009JA014326.

Newell, P. T., T. Sotirelis, and S. Wing (2010), Seasonal variations in diffuse, monoenergetic, and broadband aurora, *J. Geophys. Res.*, *115*, A03216, doi:10.1029/2009JA014805.

Ni, B., R. M. Thorne, R. B. Horne, N. P. Meredith, Y. Y. Shprits, L. Chen, and W. Li (2011a), Resonant scattering of plasma sheet electrons leading to diffuse auroral precipitation: 1. Evaluation for electrostatic electron cyclotron harmonic waves, *J. Geophys. Res.*, *116*, A04218, doi:10.1029/2010JA016232.

Ni, B., R. M. Thorne, N. P. Meredith, R. B. Horne, and Y. Y. Shprits (2011b), Resonant scattering of plasma sheet electrons leading to diffuse auroral precipitation: 2. Evaluation for whistler mode chorus waves, *J. Geophys. Res.*, *116*, A04219, doi:10.1029/2010JA016233.

Ni, B., R. Thorne, J. Liang, V. Angelopoulos, C. Cully, W. Li, X. Zhang, M. Hartinger, O. Le Contel, and A. Roux (2011c), Global distribution of electrostatic electron cyclotron harmonic waves observed on THEMIS, *Geophys. Res. Lett.*, *38*, L17105, doi:10.1029/2011GL048793.

Ni, B., J. Liang, R. M. Thorne, V. Angelopoulos, R. B. Horne, M. Kubyshkina, E. Spanswick, E. F. Donovan, and D. Lummerzheim (2012a), Efficient diffuse auroral electron scattering by electrostatic electron cyclotron harmonic waves in the outer magnetosphere: A detailed case study, *J. Geophys. Res.*, *117*, A01218, doi:10.1029/2011JA017095.

Ni, B., R. M. Thorne, and Q. Ma (2012b), Bounce-averaged Fokker-Planck diffusion equation in non-dipolar magnetic fields with applications to the Dungey magnetosphere, *Ann. Geophys.*, *30*, 733–750, doi:10.5194/angeo-30-733-2012.

Petrinec, S. M., D. L. Chenette, J. Mobilia, M. A. Rinaldi, and W. L. Imhof (1999), Statistical X ray auroral emissions-PIXIE observations, *Geophys. Res. Lett.*, *26*(11), 1565–1568, doi:10.1029/1999GL900295.

Roeder, J. L., and H. C. Koons (1989), A survey of electron cyclotron waves in the magnetosphere and the diffuse auroral electron precipitation, *J. Geophys. Res.*, *94*(A3), 2529–2541.

Roux, A., O. Le Contel, C. Coillot, A. Bouabdellah, B. de la Porte, D. Alison, S. Ruocco, and M. C. Vassal (2008), The search coil magnetometer for THEMIS, *Space Sci. Rev.*, *141*, 265–275, doi:10.1007/s11214-008-9455-8.

Tao, X., R. M. Thorne, W. Li, B. Ni, N. P. Meredith, and R. B. Horne (2011), Evolution of electron pitch-angle distributions following injection from the plasma sheet, *J. Geophys. Res.*, *116*, A04229, doi:10.1029/2010JA016245.

Thorne, R. M., B. Ni, X. Tao, R. B. Horne, and N. P. Meredith (2010), Scattering by chorus waves as the dominant cause of diffuse auroral precipitation, *Nature*, *467*, 943–946, doi:10.1038/nature09467.

Tsyganenko, N. A. (1989), A magnetospheric magnetic field model with a warped tail current sheet, *Planet. Space Sci.*, *37*, 5–20.

Tsyganenko, N. A. (1995), Modeling the Earth's magnetospheric magnetic field confined within a realistic magnetopause, *J. Geophys. Res.*, *100*(A4), 5599–5612, doi:10.1029/94JA03193.

Tsyganenko, N. A. (1996), Effects of the solar wind conditions on the global magnetospheric configuration as deduced from data-based field models, *Eur. Space Agency Spec. Publ. ESA*, *SP-389*, 181–185.

Yue, C., C.-P. Wang, S. G. Zaharia, X. Xing, and L. Lyons (2013), Empirical modeling of plasma sheet pressure and three-dimensional force-balanced magnetospheric magnetic field structure: 2. Modeling, *J. Geophys. Res. Space Physics*, *118*, 6166–6175, doi:10.1002/2013JA018943.

Zhang, X.-J., and V. Angelopoulos (2014), On the relationship of electrostatic cyclotron harmonic emissions with electron injections and dipolarization fronts, *J. Geophys. Res. Space Physics*, *119*, 2536–2549, doi:10.1002/2013JA019540.

Zhang, X.-J., V. Angelopoulos, B. Ni, R. M. Thorne, and R. B. Horne (2013), Quasi-steady, marginally unstable electron cyclotron harmonic wave amplitudes, *J. Geophys. Res. Space Physics*, *118*, 3165–3172, doi:10.1002/jgra.50319.

Zhang, X.-J., V. Angelopoulos, B. Ni, R. M. Thorne, and R. B. Horne (2014), Extent of ECH wave emissions in the Earth's magnetotail, *J. Geophys. Res. Space Physics*, *119*, 5561–5574, doi:10.1002/2014JA019931.